Biomass Conversion and Biorefinery (2019) 9:401–409
https://doi.org/10.1007/s13399-019-00378-5

ORIGINAL ARTICLE

Tofu-derived nitrogen-doped mesoporous carbon materials as metal-free catalyst for oxygen reduction reaction

Li Mu[1] · Runwei Wang[2] · Chao Tang[1]

Received: 24 August 2018 / Revised: 19 December 2018 / Accepted: 22 January 2019 / Published online: 1 February 2019

Abstract

Nitrogen dope mesoporous carbon materials are widely used in the designing of oxygen reduction reaction (ORR) catalysts. How to prepare nitrogen-doped carbons (NC) with broad mass transfer path and preserve abundant ORR active nitrogen functionalities is still a great challenge. Here, nitrogen-doped mesoporous carbon materials are obtained through simply pyrolysis a mixture of renewable biomass (tofu) and $ZnCl_2$. Owing to the effective chemical activation effect during carbonization, the optimal NC could present high porosity (high surface area of 1062 $m^2\ g^{-1}$, large pore volume of 0.97 $cm^3\ g^{-1}$) and high nitrogen content (7.74 wt%). Benefit from the rich of nitrogen functionalities to create abundant active sites and the well-developed mesoporous structure (high mesopore area 825 $m^2\ g^{-1}$ and dual mesopore system with mesopore in both 3 nm and 30 nm) to guarantee fast mass transport and electron transfer, the obtained NC could serve as fine metal-free ORR catalyst, accelerating oxygen reduction reaction via high efficient $4e^-$ oxygen reduction pathway. And more important, NC showed higher stability than commercial Pt/C (20 wt%), which highlight its great potential in the designing of electrocatalyst.

Keywords Nitrogen dope carbon · Mesoporous materials · Biomass · $ZnCl_2$ activation · Oxygen reduction reaction

1 Introduction

Oxygen reduction reaction (ORR) is the cornerstone of many sustainable energy-conversion techniques, such as fuel cell and metal air batteries [1–3]. Designing of high efficient ORR catalyst is critical for commercialization of these techniques. Traditional Pt catalysts could show high ORR activity, but the large-scale utilization of Pt catalyst is hindered by their high cost, limited reserve, and poor stability [4–6]. Recently, noble metal-free and metal-free ORR catalyst which holds ORR activity comparable with Pt is getting more and more attentions.

Owing to the fine chemical and physical properties, carbon materials are widely used in the field of energy storage and conversation [4–8]. Some recent reports have showed that precise designed nitrogen-doped carbon could show high ORR activities comparable to Pt. The ORR active sites of NC could be attributed to the existence of N functionalities. N heteroatom holds different atom size and higher electronegativity compared with carbon framework, thus could afford adjacent carbon atoms more positive charge density, which is preferable for the chemisorption of oxygen molecules and weakens the O–O bonding to promote the ORR catalytic process [9–11]. Considering multi-phases (i.e., gas reactant, liquid electrolyte, and solid catalyst) are involved in ORR process, fast mass transfer is also a critical factor influencing the total efficiency [6, 12–15]. Obviously, the narrow micropores could not meet this demand; they cannot expose active sites effectively and tend to be blocked during operation. On the contrary, wide entry mesopore or even macropores could expose all these active sites and guarantee smooth mass transport and fast electron transfer. Thus, nitrogen-doped mesoporous carbon materials (NMCs) which hold abundant ORR active sites and offer fast mass transport path are highly desired in the designing of multi-phase involved ORR electrocatalysts. Unfortunately, most carbon catalysts only show low porosity

Electronic supplementary material The online version of this article (https://doi.org/10.1007/s13399-019-00378-5) contains supplementary material, which is available to authorized users.

✉ Li Mu
mulichangchun@163.com

[1] School of Food Science and Engineering, Changchun University, Changchun 130021, China

[2] Department of Chemistry, Jilin University, Changchun 130012, China

despite complicated preparation processes are involved which normally lead to poor ORR performances. And it is still a great challenge to prepare high efficient NMC ORR catalyst through a facial and effective method [1–3].

Biomasses are considered as one of the most competitive candidates for carbon precursor, owing to several advantages. (i) Biological diversity on earth could result unique structures for porous carbon. (ii) Realize in situ doping of specific heteroatom in the derived porous carbons. (iii) The continuous bio-production guarantees the widespread and sustainable supplies for biomass [16–19]. However, only heterogeneous structured carbons showing randomly distributed heteroatoms and poor porous structures could be obtained through direct carbonization of biomass. Thus, chemical or physical activation processes are always needed to disrupt and rearrange of biomolecules to elevate porosity and distribute heteroatoms homogeneously [7, 8, 20, 21]. According to previous reports, chemical activation (KOH, $ZnCl_2$) is more effective than physical activation (CO_2, steam). However, KOH is strong corrosive to equipment and will consume excessive carbon feedstock, which will result in low yield and may lead to structure collapse. More seriously, KOH activation may cause a sharp decrease in the total nitrogen content [22], which leads to shortage of ORR active sites. In contrary, the $ZnCl_2$ activation only experiences a mild dehydration reaction. Considering that biomasses contain abundant hydrogen and oxygen elements offered by biomolecules like carbohydrates, $ZnCl_2$ activation is more suitable than KOH for biomass activation [23, 24]. Moreover, $ZnCl_2$ normally generate more mesopores [7, 8] which is urgently needed in O_2 gas involved ORR processes.

Expired food will be sent back to the factory and disposed. Considering that Tofu is a well-known cheap food in traditional Chinese diet, many expired tofu was treated like garbage previously. Thus, converting those expired tofu into value-added carbon materials is essential from both financial and environmental view [25–28]. Tofu is considered ideal protein sources, just like its soybean feedstock. This means tofu could serve as an ideal nitrogen source either [24, 25]. Unlike other biochars, which are always puzzled by the heterogeneous structure inherited from their parental biomasses, tofu is made from solution form soybean milk; thus, tofu-derived porous carbon could show homogeneous texture both structural (porosity) and composition (element distribution). Tofu can be easily converted to porous carbon, but direct carbonized tofu only shows low porosity; thus, extra agents like molten salt or KOH are involved in order to get high porosity carbon materials from tofu. Unfortunately, most reported tofu-derived carbon showed only microporous structure, which could not satisfy ORR requirement, thus could only serve as electrode for supercapacitor or Li-ion batteries [20, 21, 27–29].

Herein, we prepare NMCs through simply pyrolysis of the mixture of tofu and $ZnCl_2$. The obtained NMCs showed with high porosity presented fine mesoporous structure (mesopore surface area of 825 $m^2\ g^{-1}$ and mesopore volume of 0.88 $cm^3\ g^{-1}$). NMCs could preserve nitrogen functionalities effectively (total nitrogen content reach 7.7 wt%). And more important, a homogeneous distribution of these heteroatoms, presented majorly ORR active pyridinic-N moieties. Owing to these fascinating characteristics, the obtained nitrogen-doped porous carbon showed good ORR performance, accelerating ORR through a high efficient 4 e^- process.

2 Experimental

2.1 Synthesis of tofu-derived nitrogen-doped mesoporous carbon

Tofu was first freeze-dried to remove the dissociative water. Then, the dried tofu powder was carbonized with a certain amount of $ZnCl_2$ in Ar atmosphere under 700 °C for 1 h. Then, the products were soaked in diluted HCl solution to remove the residual $ZnCl_2$ and other metal residue, then washed with large amount of water to remove the soluble residue and dried at 80 °C for 12 h. The obtained nitrogen-doped carbon was noted according to the mass ratio of tofu and $ZnCl_2$, means DZ21 for tofu to $ZnCl_2$ 2:1, DZ11 for tofu to $ZnCl_2$ 1:1, DZ12 for tofu to $ZnCl_2$ 1:2, DZ13 for tofu to $ZnCl_2$ 1:3, DZ14 for tofu to $ZnCl_2$ 1:4, and DZ15 for tofu to $ZnCl_2$ 1:5.

2.2 Characterization

Powder XRD patterns were obtained by using a Rigaku 2550 diffractometer with Cu Ka radiation ($\lambda = 0.15418$ nm). TG-MS was performed on NETZSCH STA499F3 QMS403D\Bruker V70 under N_2 atmosphere at a heating rate of 10 °C min^{-1}. Scanning electron microscopy (SEM) was done on a Hitachi S-5200 electron microscope. Transmission electron microscopy (TEM) images were obtained from an FEI Tecnai G2 F20s-twin D573 field emission transmission electron microscope at an accelerating voltage of 200 kV. N_2 adsorption-desorption isotherms were collected at 77 K from a Micromeritics ASAP 2020 sorptometer. The samples were degassed at 200 °C for a minimum of 10 h prior to analysis. The Brunauer-Emmett-Teller (BET) surface area was calculated using the N_2 adsorption isotherm data in the relative pressure range 0.05 to 0.25. The total pore volume was obtained at a relative pressure of 0.995. Micropore volumes were determined according to the *V-t* plot method. The pore size distributions (PSDs) were obtained from the N_2 adsorption isotherms using the original density functional theory method. X-ray photoelectron spectroscopy (XPS) spectra were

acquired using an ESCALAB250 spectrometer. Raman spectroscopy was obtained from LabRAM HR Evolution.

2.3 Electrochemical measurements

The electrochemical measurements were conducted on a Bio-Logic VSP electrochemical workstation with a standard three-electrode system. A catalyst-coated glassy carbon rotating disk electrode (diameter 3 mm) was used as the working electrode, Ag/AgCl as the reference electrode (in saturated KCl solution), and Pt foil as the counter electrode. To prepare the working electrode, the as-synthesized catalyst (4 mg) was dispersed in a solution of ethanol (0.98 mL) and Nafion suspension (5 wt%, 0.02 mL) under sonication for 2 h to form a homogeneous catalyst ink. Next, the catalyst ink (0.005 mL) was placed drop wise onto a glassy carbon rotating disk electrode and dried in air. Cyclic voltammetry (CV) measurements were carried out either in N_2- or O_2-saturated 0.1 M KOH solution at a scan rate of 50 mV s^{-1}. The rotating disk electrode (RDE) tests were performed in O_2-saturated 0.1 M KOH solution at a sweep rate of 5 mV s^{-1}. All the electrochemical measurements were performed under room temperature. For comparison, the same electrochemical tests with the same loading were conducted with commercial Pt/C (20 wt% platinum, Macklin).

The Koutecky-Levich (K-L) plots (J^{-1} vs. $\omega^{1/2}$) were analyzed at various electrode potentials. The electron transfer numbers for the oxygen reduction reaction were determined from the slopes of the linear lines according to the K-L equation (Eq. 1):

$$\frac{1}{J} = \frac{1}{J_L} + \frac{1}{J_K} = \frac{1}{B\omega^{1/2}} + \frac{1}{J_K} \quad (1)$$

$$B = 0.62nFC_0(D_0)^{2/3}v^{-1/6} \quad (2)$$

$$J_K = nFkC_0 \quad (3)$$

where J is the measured current density, JK and JL are the kinetic- and diffusion-limited current densities, ω is the angular velocity of the disk ($\omega = 2\pi N$, N is the rotation speed), n is the electron transfer number, F is the Faraday constant (F = 96,485 C mol^{-1}), C_0 is the bulk concentration of O_2 ($C_0 = 1.2 \times 10^{-6}$ mol cm^{-3} in 0.1 M KOH), D_0 is diffusion coefficient of O_2 ($D_0 = 1.9 \times 10^{-5}$ cm^2 s^{-1} (in 0.1 M KOH), υ is the kinematic viscosity of the electrolyte ($\upsilon = 0.01$ cm^2 s^{-1} in 0.1 M KOH), and k is the electron transfer rate constant.

For stability tests, chronoamperometric measurements were conducted at − 0.4 V (vs. Ag/AgCl) at a rotating speed of 1600 rpm under O_2 atmosphere. The measured potentials against Ag/AgCl were then converted to RHE using the relation, in 0.1 M KOH, $E_{potential}$ vs. RHE = $E_{potential}$ vs. Ag/AgCl + 0.1989 V + 0.0592 pH).

3 Results and discussion

3.1 Structural characterization of the samples

From SEM photographs (Fig. 1 and Fig. S1) of NMCs, the direct carbonized tofu was large monolithic with rough surface, implying its dense texture. This means self-activation is not sufficient. Involve low ratio $ZnCl_2$ result insufficient activation either, only few large holes with dense surface could be observed from magnified photographs of DZ21 and DZ11.

However, after more $ZnCl_2$ was involved, as observed in SEM images of DZ13 to DZ15, cinder-like nanoparticles with fluffy surface composed of abundant large macropores and mesopores could be identified. This means more developed porosity arouse from $ZnCl_2$ activation.

Nitrogen adsorption results (Fig. 1 and Table S2) confirmed the evolution of porosity. The direct carbonized tofu showed dense structure with ultra-low surface area of 2.2 m^2 g^{-1}. After $ZnCl_2$ was involved, the BET surface area increased significantly reaching a high value of 612 m^2 g^{-1}(DZ21) and the total pore volume also increased to 0.30 cm^3 g^{-1}. Further elevate $ZnCl_2$ ratio will endow more developed porosity. After optimization, BET surface area and total pore volume could be elevated to ultra-high values of 1173 m^2 g^{-1} and 0.94 cm^3 g^{-1}, respectively. More important, a more obviously change could be identified from their porous structures, viz. from microporous to mesoporous structure. DZ21 and DZ11 possessed similar type I isotherms which means typical microporous structure. After more $ZnCl_2$ was involved, the pore gradually expanded into mesopore scale (from DZ12 to DZ15) as reflected by the presenting of type IV isotherms (proof of mesoporous structure). DZ12 and DZ13 showed similar isotherms (type IV isotherm with H4 hysteresis loop), which means coexistence of mesopore and micropores. DZ21 possessed ultra-low mesopore volume of only 0.04 cm^3 g^{-1}, while DZ13 showed high mesopore volume of 0.68 cm^3 g^{-1}. The dramatic increase of mesopores confirmed the effective reaming effect for $ZnCl_2$. The pore structure changed more significantly when we further elevate $ZnCl_2$ ratio. DZ14 and DZ15 presented type IV isotherm with H3 hysteresis loop. These results mean that DZ14 and DZ15 possessed widespread pore size distribution contained both micropores, mesopores, and macropores.

Micropore volume of DZ14 was only 0.10 cm^3 g^{-1}, which is much lower than DZ21 (0.26 cm^3 g^{-1}). On the contrary, DZ14 showed ultra-high mesopore volume of 0.88 cm^3 g^{-1}, which is obviously far beyond that of DZ21 (0.04 cm^3 g^{-1}), and highlighted the reaming effect of $ZnCl_2$. The drop in mesopore volume from DZ14 to DZ15 implied the collapse of porous structure caused by over activation due to the involving of excessive amount of $ZnCl_2$. DFT pore size distribution further confirmed our analysis. Despite DZ21 and DZ11 contained mainly micropore (2 nm), all the other NMCs presented dual mesopores concentrated in 3 nm and

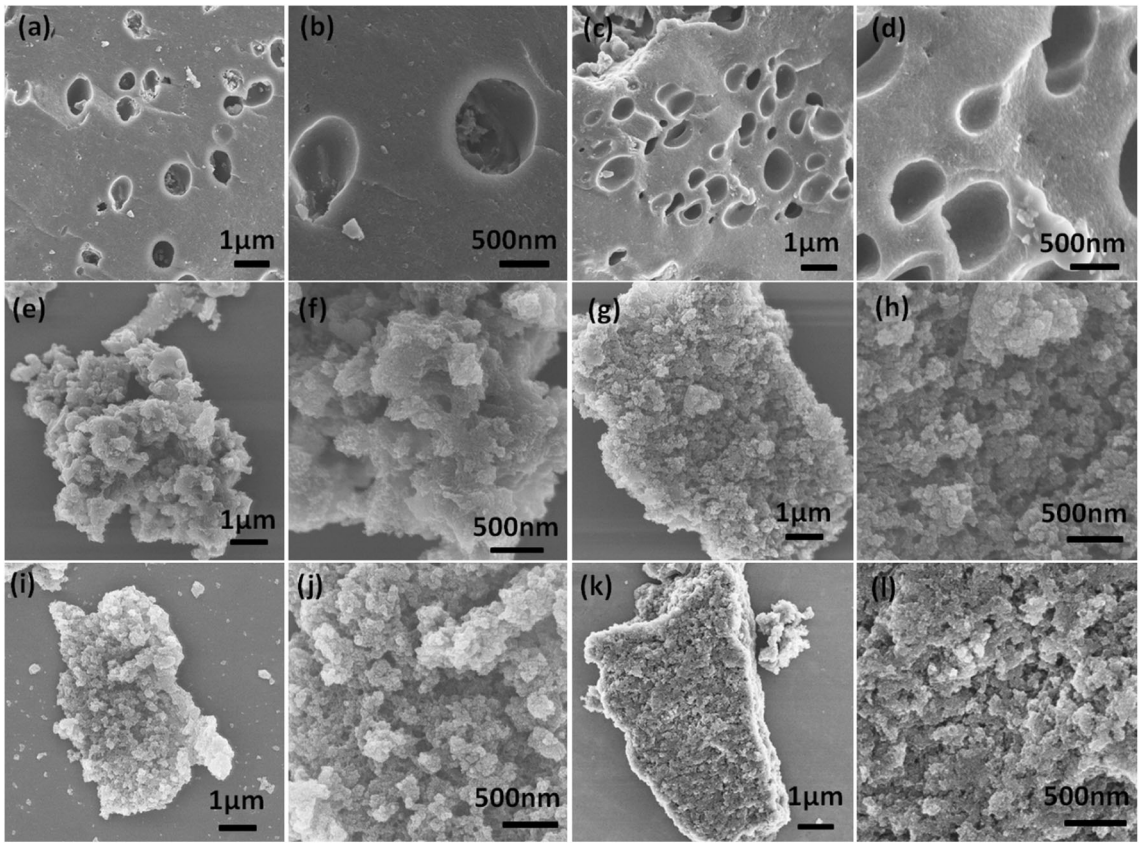

Fig. 1 SEM images of nitrogen-doped porous carbon. **a**, **b** DZ21, **c**, **d** DZ11, **e**, **f** DZ12, **g**, **h** DZ13, **i**, **j** DZ14, **k**, **l** for DZ15

30 nm. This further confirmed the successfully incorporation of mesopores in NMCs by $ZnCl_2$ activation.

To get more information about the texture characters of NMCs, TEM and XPS were also performed. TEM images (Fig. 3) confirmed that NMCs possessed homogeneous textures with well-developed porous structure. DZ21 and DZ11 were integral monolithic and large amount of micropores could be the identified from their magnified TEM images. This is consistent with N_2 sorption results, which further confirmed their microporous structures. On the contrary, DZ12 to DZ15 presented fluffy structures with abundant mesopores. Combined with the SEM and nitrogen adsorption results, we confirmed that $ZnCl_2$ activation did afford these samples with fine mesoporous structure. To note, unlike other biochars which will inherit the undesirable micro structure of their parental biomass, no structure separation could be observed in NMCs. Both micropores and mesopores were distributed homogeneously, which attribute to the homogeneous construction of tofu precursor and the $ZnCl_2$ activation afforded atoms rearrangement, thus highlighting the advantage of choosing tofu as carbon precursor.

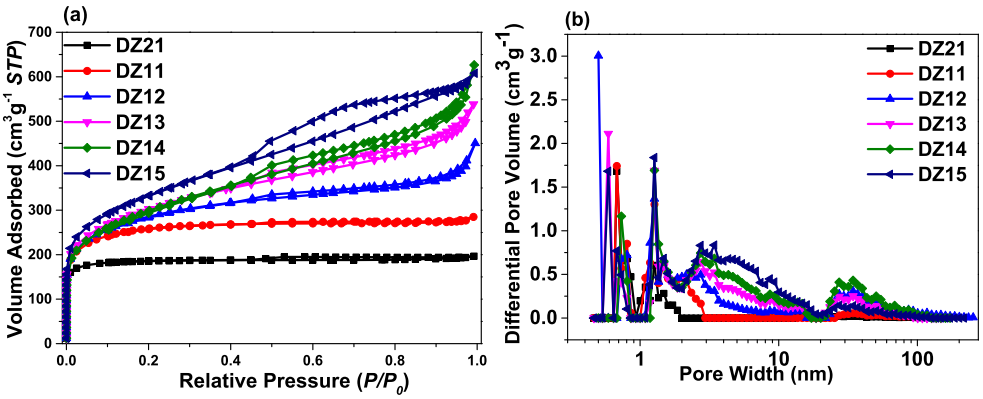

Fig. 2 **a** Nitrogen adsorption-desorption isotherms and **b** pore size distribution curves

Table 1 Textural properties of nitrogen-doped porous carbon

Name	BET (m^{-2} g)	V_{Total} (cm^{-3} g)	S_{micro} (m^{-2} g)	V_{micro} (cm^{-3} g)	S_{meso} (m^{-2} g)	V_{meso} (cm^{-3} g)
DZ21	612	0.30	545	0.26	66	0.04
DZ11	883	0.44	575	0.26	308	0.15
DZ12	996	0.70	410	0.18	585	0.49
DZ13	1061	0.83	332	0.15	677	0.68
DZ14	1062	0.97	236	0.10	825	0.88
DZ15	1173	0.94	297	0.13	876	0.82

Element analysis (Table S1) revealed that NMCs could preserve nitrogen heteroatoms effectively (> 5 wt%). And the total nitrogen content could even reach high values of 7.74 wt%. Unlike the dramatic changes in porosity, variation of $ZnCl_2$ ratio did not affect total nitrogen amount significantly, but nitrogen content still varied in a small range. Though $ZnCl_2$ activation process experienced merely dehydration (only hydrogen and oxygen atoms participate), the biomolecules in tofu contain so large content of hydrogen and oxygen, which means removal of these atoms will also disturb the total framework and further cause the rearrangement of residual atoms, viz. C and N.

Thus, variation of $ZnCl_2$ content will also affect N functionalities, which also contribute to the homogeneous distribution of nitrogen heteroatom (Fig. S2). Nitrogen content was calculated from XPS spectra corresponding well with element analysis. High-resolution N1s spectra (Fig. 4) revealed that these samples contained similar nitrogen function groups either. Briefly, three types of nitrogen, i.e., pyrollic-N, pyridinic-N, and graphitic-N, could be distinguished [30–35]. Pyrollic-

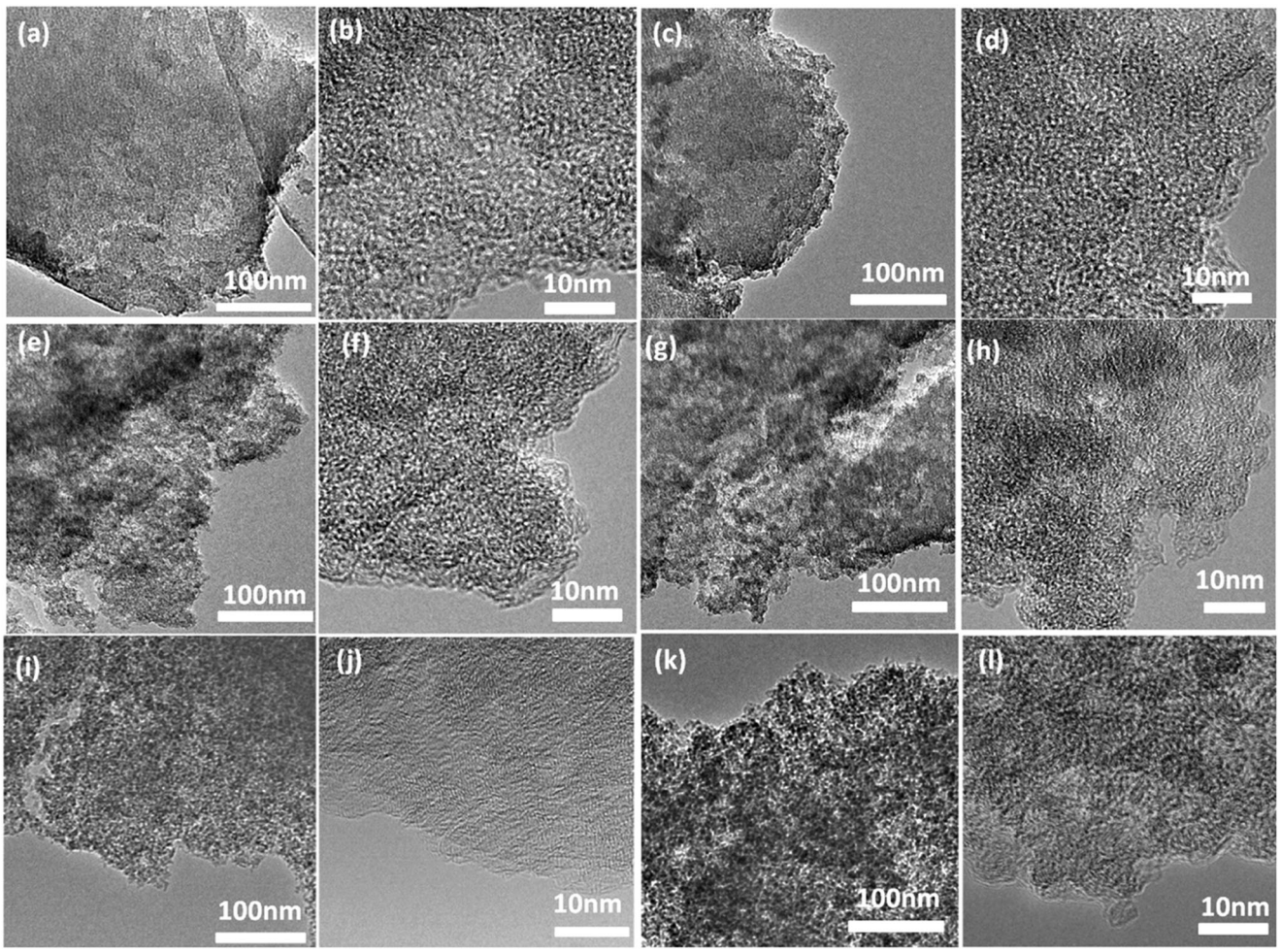

Fig. 3 TEM images of nitrogen-doped porous carbon, DZ21 (**a**, **b**), DZ11 (**c**, **d**), DZ12 (**e**, **f**), DZ13 (**g**, **h**), DZ14 (**i**, **j**), and DZ15 (**k**, **l**

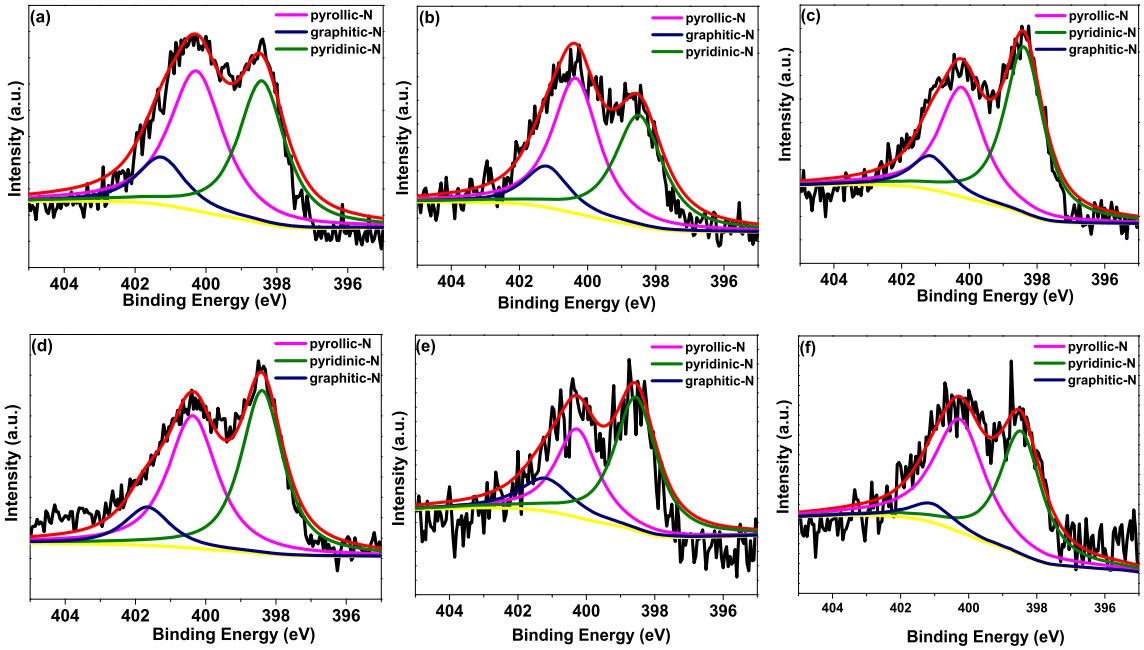

Fig. 4 XPS spectrum nitrogen species for **a** DZ21, **b** DZ11, **c** DZ12, **d** DZ13, **e** DZ14, and **f** DZ15

N and pyridinic-N are major nitrogen forms. The lacking of most stable graphitic-N is attributed to the existence of high content heteroatoms and the rearrangement of atoms during $ZnCl_2$ activation, which could be confirmed by the high I_D/I_G ratio ($I_D/I_G > 1$, Fig. S3) of NMCs. Fortunately, the hydrophilic pyrollic-N groups could guarantee smooth penetration of aqueous electrolyte in carbon catalyst, to make it more suitable catalyst to operate in aqueous solution involved applications. More important, pyridinic-N could afford adjacent carbon atoms more positive charge density, which is preferable for the chemisorption of oxygen molecules and weakens the O–O bonding to promote the ORR catalytic process, thus is favorable for ORR [9–11, 36, 37].

Raman spectrum (Fig. S3) of NMCs showed high I_D/I_G ratio ($I_D/I_G > 1$) confirming the amorphous texture containing majorly disordered skeletons. The high disordered carbon frameworks for NMCs arouse from in situ doped nitrogen along with defects and edges introduced by chemical activation. To note, some literature reported that defect and edges of carbon frameworks could also serve as ORR active sites to show considerable ORR activity either [1, 38, 39]. Thus, the high I_D/I_G ratio obtained in NMCs means they may present high ORR activity.

3.2 Catalytic performance of nitrogen-doped porous carbon as the electrocatalyst for ORR

Based on their structure and texture information, we explored the ORR activity of NMCs. CV measurement was first performed to test their potential ORR activities. NMCs showed pseudo-rectangle-shaped CV curves in N_2 saturated 0.1 M KOH electrolyte (Fig. 5, S4) and no obvious peaks could be observed. In contrary, strong redox peaks emerged at around 0.8 V (vs. RHE) in O_2 saturate 0.1 M KOH electrolyte. The strong contrast before and after introduction of O_2 means the redox peaks are attributed to the reducing of oxygen molecule, which confirmed the high ORR activity of NMCs.

LSV tests (Fig. 5) revealed that at a rotating speed of 1600 rpm, DZ21 showed inferior ORR activity presented a negative onset potential of 0.781 V (vs. RHE). Luckily, the onset potentials showed positive shifts for the residual samples. This is consistent with the positive shift of their redox peaks in CV curves. Nitrogen functionalities and porous structures are main factors affecting the ORR performance of metal-free catalyst. Considering that NMCs held similar nitrogen composition (both N amount and chemical forms), they should hold similar amount active sites. Thus, we attributed their different performances to the changes in porosity. In fact, the variation of ORR activities did showed strong relevance to the development of porosity in NMCs. When the BET surface area increased from 612 m^{-2} g (DZ21) to 1173 m^{-2} g (DZ15), the onset potential showed positive shifts, from 0.78 V (vs. RHE DZ21) to high values of 0.894 V (vs. RHE for DZ14). However, the onset potential downshifted to 0.884 V (vs. RHE more negative in DZ15). This means BET surface area may not be the dominant factor influencing the ORR activity. However, the changes in ORR activity showed strong correlations with mesopore amount. As we described before, DZ14 held the highest mesopore volume, while over activation will cause structure collapse, leading to a significant drop of mesopores in DZ15 (especially for mesopores in the range of 20 to 50 nm Fig. 2, Table 1). The decrease in mesopores

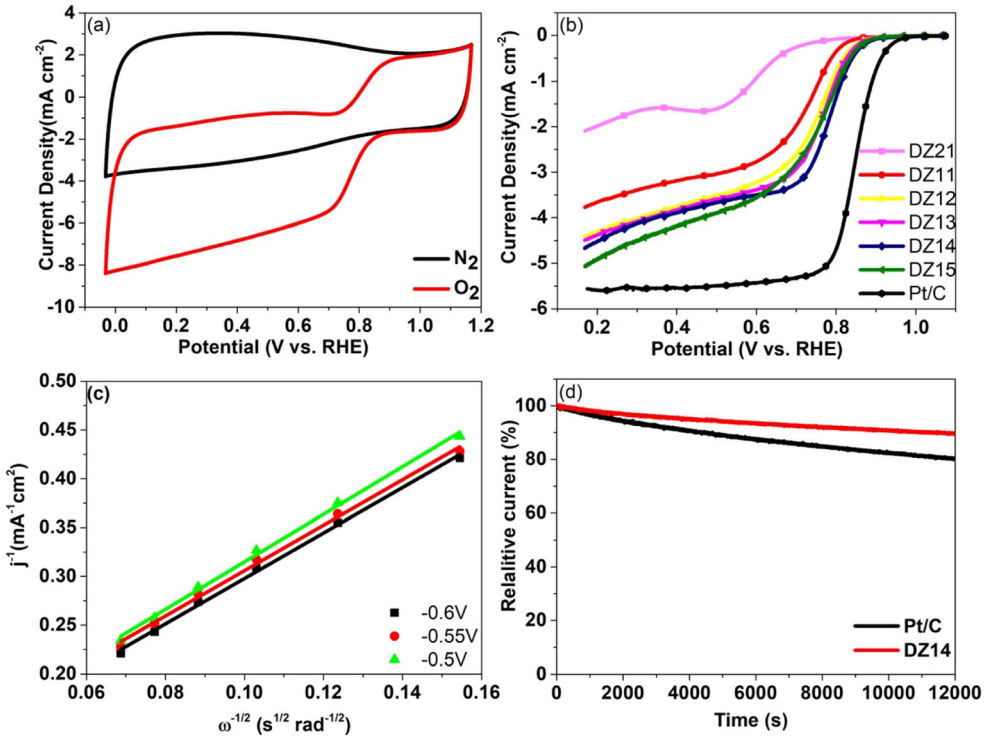

Fig. 5 **a** CV curves for DZ14 in 0.1 M KOH electrolyte. **b** LSV plots for nitrogen-doped porous carbon and 20 wt% Pt/C. **c** Koutecky-Levich (K-L) plots for DZ14 at different potentials. **d** Chronopotentiometry test for DZ14 and Pt/C 20 wt%

means limited reactant transport path. Besides, over activation also result in a decrease of nitrogen species in DZ15 (especially catalytic active pyridinic-N moieties, Table S1), which will obviously drag the ORR activity. While the onset potential for DZ14 is close to commercial Pt/C (20 wt%) catalyst and superior than many nitrogen-doped carbons reported in literature, like mesoporous nitrogen-doped carbon microfibers [40], nanoshell carbon co-doped with boron and nitrogen [41], three-dimensional nitrogen-doped graphene [42], and nitrogen-doped graphene anchored cobalt oxides [43] suggests it's fine ORR catalytic activity.

To give deep insight into the reaction mechanism, we then conducted RDE test to collect LSV curves of DZ14 at different rotating. LSV curves showed that limiting current density increased almost linearly from 225 to 2025 rpm, corresponding to the previous reports that diffusion distance could be shortened at higher rotation rates. The linearity of K-L plots suggests first-order reaction kinetics toward the concentration of dissolved oxygen [17, 22, 44]. The electrons transferred number (n) per O_2 was calculated from the slopes of K-L equation. Electrons transferred per O_2 (n) of DZ14 were 3.9 (at − 0.6 V (vs. Ag/AgCl)), 3.91 (at − 0.55 V (vs. Ag/AgCl)), and 3.73 (at − 0.5 V (vs. Ag/AgCl)). This means the reduction of oxygen processes in DZ14 experienced a high efficient $4e^-$ pathway. Besides the high activity, stability is another key parameter in elevate catalyst. Durability test shows that after 12,000 s continuing operation, only 80% of the initial current could be maintained in commercial Pt/C catalyst. However, high current retention of 90% could be realized from DZ14, suggesting the superior stability comparing with commercial Pt/C catalyst.

4 Conclusion

In summary, we prepared N-doped mesoporous carbons (NMCs) using tofu as precursor and through $ZnCl_2$ activation process. The porosity for these porous carbon materials can be conveniently controlled by simply regulation $ZnCl_2$ ratio. After optimization, tofu-derived NMCs could show high mesoporous porosity with homogeneous distribution of nitrogen functionalities. As a result, DZ14 presented high ORR activity, experiencing a high efficient $4e^-$ ORR path and showed better stability than Pt/C. Except for presenting a satisfied metal-free ORR electrocatalyst, the comprehensive research in this paper will also promote the development of biomass-derived carbon electrocatalyst.

Funding information This study received funding from the Education Department of Jilin Province (2016299).

References

1. Jia Y, Zhang L, Du A et al (2016) Defect graphene as a trifunctional catalyst for electrochemical reactions. Adv Mater 28:9532–9538
2. Wang R, Wang K, Wang Z, Song H, Wang H, Ji S (2015) Pig bones derived N-doped carbon with multi-level pores as electrocatalyst for oxygen reduction. J Power Sources 297:295–301
3. Wang R, Wang H, Zhou T, Key J, Ma Y, Zhang Z, Wang Q, Ji S (2015) The enhanced electrocatalytic activity of okara-derived N-

doped mesoporous carbon for oxygen reduction reaction. J Power Sources 274:741–747
4. You C, Zheng R, Shu T, Liu L, Liao S (2016) High porosity and surface area self-doped carbon derived from polyacrylonitrile as efficient electrocatalyst towards oxygen reduction. J Power Sources 324:134–141
5. Liang HW, Zhuang X, Brüller S et al (2014) Hierarchically porous carbons with optimized nitrogen doping as highly active electrocatalysts for oxygen reduction. Nat Commun 5:4973
6. Pampel J, Fellinger TP (2016) Opening of bottleneck pores for the improvement of nitrogen doped carbon electrocatalysts. Adv Energy Mater 6:1502389
7. Zhang LY, Wang MR, Lai YQ, Li XY (2017) Nitrogen-doped microporous carbon: an efficient oxygen reduction catalyst for Zn-air batteries. J Power Sources 359:71–79
8. Ludwinowicz J, Jaroniec M (2015) Effect of activating agents on the development of microporosity in polymeric-based carbon for CO_2 adsorption. Carbon 94:673–679
9. Xing T, Zheng Y, Li LH, Cowie BCC, Gunzelmann D, Qiao SZ, Huang S, Chen Y (2014) Observation of active sites for oxygen reduction reaction on nitrogen-doped multilayer graphene. ACS Nano 8:6856–6862
10. Yang HB, Miao J, Hung SF, Chen J, Tao HB, Wang X, Zhang L, Chen R, Gao J, Chen HM, Dai L, Liu B (2016) Identification of catalytic sites for oxygen reduction and oxygen evolution in N-doped graphene materials: development of highly efficient metal-free bifunctional electrocatalyst. Sci Adv 2:e1501122
11. Guo D, Shibuya R, Akiba C et al (2016) Active sites of nitrogen-doped carbon materials for oxygen reduction reaction clarified using model catalysts. Science 351:362–365
12. Lee S, Choun M, Ye Y, Lee J, Mun Y, Kang E, Hwang J, Lee YH, Shin CH, Moon SH, Kim SK, Lee E, Lee J (2015) Designing a highly active metal-free oxygen reduction catalyst in membrane electrode assemblies for alkaline fuel cells: effects of pore size and doping-site position. Angew Chem Int Ed 54:9230–9234
13. Zheng Y, Jiao Y, Qiao SZ (2015) Engineering of carbon-based electrocatalysts for emerging energy conversion: from fundamentality to functionality. Adv Mater 27:5372–5378
14. Tian GL, Zhang Q, Zhang B, Jin YG, Huang JQ, Su DS, Wei F (2014) Toward full exposure of "active sites": nanocarbon electrocatalyst with surface enriched nitrogen for superior oxygen reduction and evolution reactivity. Adv Funct Mater 24:5956–5961
15. Tang J, Liu J, Li C, Li Y, Tade MO, Dai S, Yamauchi Y (2015) Synthesis of nitrogen-doped mesoporous carbon spheres with extra-large pores through assembly of diblock copolymer micelles. Angew Chem Int Ed 54:588–593
16. Wang Q, Li Y, Wang K, Zhou J, Zhu L, Gu L, Hu J, Cao X (2017) Mass production of porous biocarbon self-doped by phosphorus and nitrogen for cost-effective zinc–air batteries. Electrochim Acta 257:250–258
17. Cao L, Lin Z, Huang J, Yu X, Wu X, Zhang B, Zhan Y, Xie F, Zhang W, Chen J, Xie W, Mai W, Meng H (2017) Nitrogen doped amorphous carbon as metal free electrocatalyst for oxygen reduction reaction. Int J Hydrog Energy 42:876–885
18. Zheng X, Cao X, Li X, Tian J, Jin C, Yang R (2017) Biomass lysine-derived nitrogen-doped carbon hollow cubes via a NaCl crystal template: an efficient bifunctional electrocatalyst for oxygen reduction and evolution reactions. Nanoscale 9:1059–1067
19. Li X, Fang Y, Zhao S, Wu J, Li F, Tian M, Long X, Jin J, Ma J (2016) Nitrogen-doped mesoporous carbon nanosheet/carbon nanotube hybrids as metal-free bi-functional electrocatalysts for water oxidation and oxygen reduction. J Mater Chem A 4:13133–13141
20. Ouyang T, Cheng K, Gao Y, Kong S, Ye K, Wang G, Cao D (2016) Molten salt synthesis of nitrogen doped porous carbon: a new preparation methodology for high-volumetric capacitance electrode materials. J Mater Chem A 4:9832–9843
21. Lee DY, An GH, Ahn HJ (2017) High-surface-area tofu based activated porous carbon for electrical double-layer capacitors. J Ind Eng Chem 52:121–127
22. Wang Y, Pan Y, Zhu L, Guo N, Wang R, Zhang Z, Qiu S (2019) Structure regulation of amino acids derived nitrogen doped porous carbon nanosheet through facile solid state assembly method. Microporous Mesoporous Mater 277:36–44
23. Boyjoo Y, Cheng Y, Zhong H, Tian H, Pan J, Pareek VK, Jiang SP, Lamonier JF, Jaroniec M, Liu J (2017) From waste Coca Cola® to activated carbons with impressive capabilities for CO2 adsorption and supercapacitors. Carbon 116:490–499
24. Yue Z, Mangun CL, Economy J (2002) Preparation of fibrous porous materials by chemical activation: 1. ZnCl2 activation of polymer-coated fibers. Carbon 40:1181–1191
25. Rossi F, Felis GE, Martinelli A, Calcavecchia B, Torriani S (2016) Microbiological characteristics of fresh tofu produced in small industrial scale and identification of specific spoiling microorganisms (SSO). LWT-Food Sci Technol 70:280–285
26. Zhu Q, Wu F, Saito M, Tatsumi E, Yin L (2016) Effect of magnesium salt concentration in water-in-oil emulsions on the physical properties and microstructure of tofu. Food Chem 201:197–204
27. Sun X, Ye J, Pan F, Xu J, Cheng T, Wang X, Ikram M, Zhu Y (2018) Hierarchical porous carbon obtained from frozen tofu for efficient energy storage. New J Chem 42:12421–12428
28. An GH, Lee DY, Ahn HJ (2017) Tofu-derived carbon framework with embedded ultrasmall tin nanocrystals for high-performance energy storage devices. J Alloys Compd 722:60–68
29. Wang H, Wang C, Xiong Y et al (2017) Simple synthesis of N-doped interconnected porous carbon from Chinese tofu for high-performance supercapacitor and lithium-ion battery applications. J Electrochem Soc 164:A3832–A3839
30. Ai K, Liu Y, Ruan C, Lu L, Lu GM (2013) Sp^2 C-dominant N-doped carbon sub-micrometer spheres with a tunable size: a versatile platform for highly efficient oxygen-reduction catalysts. Adv Mater 25:998–1003
31. Shen M, Zheng LR, He W, Ruan C, Jiang C, Ai K, Lu L (2015) High-performance oxygen reduction electrocatalysts derived from uniform cobalt-adenine assemblies. Nano Energy 17:120–130
32. Jeon I, Zhang S, Zhang L, Choi H, Seo J, Xia Z, Dai L, Baek J (2013) Edge-selectively sulfurized graphene nanoplatelets as efficient metal-free electrocatalysts for oxygen reduction reaction: the electron spin effect. Adv Mater 25:6138–6145
33. Dai L, Xue Y, Qu L, Choi HJ, Baek JB (2015) Metal-free catalysts for oxygen reduction reaction. Chem Rev 115:4823–4892
34. Wang Y, Zou H, Zeng S, Pan Y, Wang R, Wang X, Sun Q, Zhang Z, Qiu S (2015) A one-step carbonization route towards nitrogen-doped porous carbon hollow spheres with ultrahigh nitrogen content for CO_2 adsorption. Chem Commun 51:12423–12426
35. Gao S, Geng K, Liu H, Wei X, Zhang M, Wang P, Wang J (2015) Transforming organic-rich amaranthus waste into nitrogen-doped carbon with superior performance of the oxygen reduction reaction. Energy Environ Sci 8:221–229
36. Jiao Y, Zheng Y, Jaroniec M, Qiao SZ (2014) Origin of the electrocatalytic oxygen reduction activity of graphene-based catalysts: a roadmap to achieve the best performance. J Am Chem Soc 136:4394–4403
37. Zhao Z, Li M, Zhang L, Dai L, Xia Z (2015) Design principles for heteroatom-doped carbon nanomaterials as highly efficient catalysts for fuel cells and metal-air batteries. Adv Mater 27:6834–6840
38. Tang C, Zhang Q (2017) Nanocarbon for oxygen reduction electrocatalysis: dopants, edges, and defects. Adv Mater 29:1604103
39. Xia W, Mahmood A, Liang Z, Zou R, Guo S (2016) Earth-abundant nanomaterials for oxygen reduction. Angew Chem Int Ed 55:2650–2676

40. Kong A, Fan X, Chen A, Zhang H, Shan Y (2017) Mesoporous nitrogen-doped carbon microfibers derived from Mg-biquinoline-dicarboxy compound for efficient oxygen electroreduction. J Solid State Chem 246:399–403
41. Ishii T, Maie T, Kimura N, Kobori Y, Imashiro Y, Ozaki JI (2017) Enhanced catalytic activity of nanoshell carbon co-doped with boron and nitrogen in the oxygen reduction reaction. Int J Hydrog Energy 42:15489–15496
42. Lu X, Li Z, Yin X, Wang S, Liu Y, Wang Y (2017) Controllable synthesis of three-dimensional nitrogen-doped graphene as a high performance electrocatalyst for oxygen reduction reaction. Int J Hydrog Energy 42:17504–17513
43. Wang Q, Hu W, Huang Y (2017) Nitrogen doped graphene anchored cobalt oxides efficiently bi-functionally catalyze both oxygen reduction reaction and oxygen revolution reaction. Int J Hydrog Energy 42:5899–5907
44. Wang Y, Pan Y, Zhu L, Guo N, Wang R, Zhang Z, Qiu S (2018) Fabrication of 3D heteroatom-doped porous carbons from self-assembly of chelate foams via a solid state method. Inorg Chem Front 5:656–664